energies

MDPI

Article

Frost Suppression and Enhancement of an Air-Source Heat Pump via an Electrostatically Sprayed Superhydrophobic Heat Exchanger

Sicheng Fan [1,2,†], Zhengyu Duan [2,†], Zhaoqing Ke [2], Donghua Zou [2,*] and Zhiping Yuan [1,*]

[1] School of Mechanical Engineering, Beijing Institute of Technology, Beijing 100081, China; fansicheng2@gmail.com
[2] School of Advanced Manufacturing, Nanchang University, Nanchang 330031, China
* Correspondence: zoudonghua@ncu.edu.cn (D.Z.); nikolatesal@live.com (Z.Y.)
† These authors contributed equally to this work.

Abstract

Frost accumulation on heat exchangers severely limits the efficiency and reliability of air-source heat pumps (ASHPs) in cold, humid environments. Superhydrophobic coatings fabricated via electrostatic spraying offer a promising energy-free strategy for frost suppression. In this study, a robust superhydrophobic coating was deposited on the heat exchanger of a residential ASHP using this scalable technique. Under low-temperature heating conditions (2/1 °C), the coated exchanger delayed frost completion by a factor of 2.83 and shortened defrosting time by 33.3% compared to a conventional hydrophilic counterpart. These improvements translated to a 6.24% increase in average heating capacity and a 2.83% gain in the coefficient of performance (COP). Although the thicker superhydrophobic coating resulted in a marginal 3.1% reduction in cooling capacity during free-cooling operation, the significant enhancements in frost resistance and heating performance underscore its practical value. This work demonstrates that electrostatic spraying is a viable and effective method for fabricating high-performance superhydrophobic heat exchangers, paving the way for more efficient and frost-resistant ASHPs.

Keywords: air-source heat pumps (ASHPs); superhydrophobic coating; electrostatic spraying; frost suppression; heating capacity; low-temperature environments; heat exchanger; coefficient of performance (COP)

Check for updates

Academic Editor: Mahmoud Bourouis

Received: 17 November 2025
Revised: 7 January 2026
Accepted: 8 January 2026
Published: 10 January 2026

Copyright: © 2026 by the authors. Licensee MDPI, Basel, Switzerland. This article is an open access article distributed under the terms and conditions of the Creative Commons Attribution (CC BY) license.

1. Introduction

Frost formation on the outdoor heat exchanger poses a significant challenge to the operation of ASHPs in cold and humid climates. The frost layer acts as a thermal insulator, leading to decreased heating efficiency, increased energy consumption, and unstable operation [1–3]. Developing efficient defrosting technologies is therefore crucial for improving energy efficiency and expanding the application of ASHPs as a sustainable heating solution [4–6].

Conventional defrosting techniques—including reverse-cycle defrosting [7], hot gas bypass defrosting [8], electric auxiliary heating [9], and thermal storage defrosting [10] all rely on external energy input, which inevitably reduces the overall energy efficiency of the system. In contrast, superhydrophobic coatings have garnered significant research interest as a passive anti-frosting strategy, capable of delaying frost formation without additional energy consumption [11,12]. The anti-icing mechanism of these coatings is

primarily attributed to their extremely low surface energy [13] and tailored micro–nano structures, which minimize the solid–liquid contact area, thereby reducing ice adhesion strength and prolonging the ice formation period [14–17].

Recent research has made significant progress in developing superhydrophobic coatings specifically for heat exchanger applications. Mao et al. [18] developed a scalable robust photothermal superhydrophobic coating with a three-level hierarchical micro/nano/sub-nano structure, demonstrating excellent anti-icing/de-icing performance in simulated/real environments. The coating maintained superhydrophobicity (contact angle >150°) and mechanical robustness even after extensive testing, with a freezing delay time increase by 46 times compared to conventional surfaces. Similarly, Yang et al. [19] fabricated a durable photothermal superhydrophobic coating using a one-step spraying method, achieving a contact angle of 160.1° and a sliding angle of 2.1°. The coating exhibited outstanding anti-/de-icing performance, with ice-melting starting within 18 s under specific conditions. For heat exchanger applications specifically, Sui et al. [12] investigated superhydrophobic microchannel heat exchangers for electric vehicle heat pumps. Their experimental results showed that after 30 min of operation, the frost thickness on the superhydrophobic-coated heat exchanger was approximately 0.4 mm, compared to 0.8 mm on uncoated surfaces. This reduction in frost accumulation led to a 48.7% reduction in heating power consumption and extended the driving range by 8.99%.

However, the practical application of conventional superhydrophobic coatings is often limited by poor durability. Their delicate micro–nano structures are susceptible to damage under mechanical stress or condensation in low-temperature, high-humidity environments, resulting in the loss of superhydrophobicity and anti-icing functionality [20,21]. Moreover, traditional fabrication methods such as chemical etching [22], laser etching [23], dip coating [24], and conventional spraying [25] are often associated with high costs, environmental concerns, and complex processing, which hinder their large-scale industrial application [26,27].

Electrostatic spraying offers a compelling alternative. Its key advantage lies in the ability to easily construct hierarchical micro–nano structures with suitable roughness [28–30], yielding coatings with superior durability, abrasion resistance, environmental friendliness, and cost-effectiveness [31,32], Liu et al. [33] developed a novel approach combining substrate heating with silane coupling agents (KH550) modification for PVDF/carbon black electrostatic spraying coatings. The resulting coatings exhibited exceptional performance with a contact angle of 162° ± 3° and a sliding angle of 4° ± 1°, while maintaining excellent mechanical and chemical durability.

While previous research on heat exchangers has extensively explored various hydrophilic and hydrophobic coatings [34,35], few studies have investigated superhydrophobic coatings under representative heat pump operating conditions. Moreover, existing studies often employ methods like boiling water treatment followed by vapor deposition to create superhydrophobic surfaces on aluminum [36,37]. These coatings typically exhibit poor abrasion resistance and chemical durability, limiting their commercial viability. Additionally, while some studies have reported improved frost delay and reduced defrosting time, the actual energy savings and emissions reduction potential of superhydrophobic heat exchangers in practical applications remain inadequately quantified.

Therefore, developing a superhydrophobic coating with physical and chemical robustness comparable to commercial hydrophilic coatings is key to enabling the widespread use of this technology in heat exchangers.

In this study, we address these research gaps through the following key innovations: resolving the core bottlenecks in the application of superhydrophobic coatings to heat exchangers in air-source heat pumps—namely, insufficient durability, challenges in large-

scale manufacturing, and a lack of system-level energy efficiency validation. Using a novel coating system based on ethylene-tetrafluoroethylene copolymer and an optimized electrostatic spraying process, a superhydrophobic functional layer with excellent mechanical strength and chemical stability was constructed on the surface of the heat exchanger. Compared to traditional methods, this technical approach significantly enhances the coating's adhesion, wear resistance, and corrosion resistance, making it better suited for the harsh demands of actual operating conditions. The uniqueness of this study lies in the first-time application of ETFE-based superhydrophobic coatings via electrostatic spraying technology to a full-scale residential air-source heat pump system, with system-level performance evaluations conducted under representative and realistic operating conditions, such as low-temperature heating and free cooling. Additionally, this study introduces an improved comprehensive energy efficiency evaluation framework that quantifies the energy benefits of both passive frost suppression and active defrosting, providing a more comprehensive assessment of the energy-saving potential of superhydrophobic heat exchangers. Therefore, this work not only proposes a superhydrophobic coating preparation method with high potential for engineering applications but, more importantly, provides critical data support and theoretical references for the reliable application of superhydrophobic technology in the field of heat pumps through system-level experimental design and evaluation methods. It holds significant guiding importance for advancing this technology from the laboratory to commercialization.

2. Materials and Methods

2.1. Experimental Materials

The experimental subject was a 1.5-horsepower residential air conditioner (Midea KFR-35GW/N8MX, Foshan, China) purchased from Media. Its heat exchanger is a single-row fin-and-tube type, with fins made of 3003 aluminums in a plain configuration. The fin spacing is 1.2 mm, and the fin width is 22 mm. The superhydrophobic coating was prepared using ETFE-Fluorine modified SiO_2 (ETFE-F-SiO_2) composite powder purchased from Beijing Droplet Leaping Technology Co., Ltd. (Beijing, China), applied to the heat exchanger surface via electrostatic spraying. The hydrophilic heat exchanger used for comparison complies with the Chinese national standard JB/T 11525-2013. Other reagents used in the experiment included anhydrous ethanol (purchased from Macklin, Shanghai, China) and deionized water produced in the laboratory (resistivity: 18 MΩ · cm).

2.2. Fabrication of Superhydrophobic Heat Exchanger Samples

The bare aluminum heat exchanger underwent sequential cleaning to remove surface contaminants. The process began with nitrogen purging, followed by ultrasonic cleaning in anhydrous ethanol and deionized water, and was completed by oven drying at 60 °C for 30 min. After cleaning, the exchanger was vertically mounted and grounded in an electrostatic spray booth. A linear spray gun operated at 60 kV and 60 μA was used to deposit ETFE-F-SiO_2 powder onto the fin surfaces by electrostatic attraction, with the powder feed rate and atomizing air pressure optimized to ensure uniform fluidization and deposition. The coated sample was then subjected to a two-stage curing process: preheating at 100 °C for 10 min, followed by curing at 280 °C for 20 min to achieve complete cross-linking. The final superhydrophobic heat exchanger was obtained after gradual cooling inside the oven. The fabrication progress of superhydrophobic Heat Exchanger is illustrated in Figure 1.

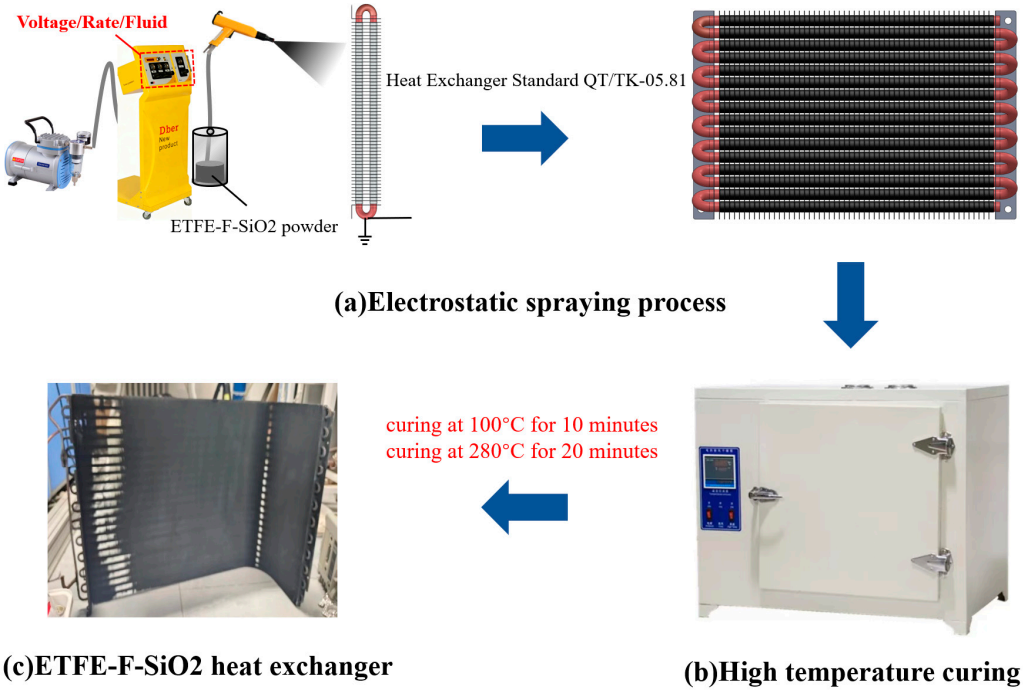


Figure 1. Fabrication process of the superhydrophobic heat exchanger by electrostatic spraying: (**a**) electrostatic spraying setup, (**b**) thermal curing (specified temperature and time), and (**c**) the final ETFE-F-SiO_2 coated sample.

2.3. Coating Characterization and Performance Evaluation

To ensure consistency, the coatings were first deposited on 100 µm thick 3003 aluminum foils under identical electrostatic spraying conditions. The coated samples were then characterized in terms of surface morphology (field-emission scanning electron microscopy), hydrophobicity (water contact angle measured with a 10 µL droplet; average of three tests), and coating thickness (metallographic microscopy). The performance of the coatings was further evaluated through chemical resistance (acid/alkali immersion, GB/T 9274 [38]), environmental durability (neutral salt spray test per GB/T 10125 [39] and accelerated UV aging per GB/T 16422.3 [40]), and mechanical properties (cupping test GB/T 4156 [41], cross-cut adhesion test GB/T 9286 [42], and T-bend test).

The coated aluminum foil samples exhibited outstanding performance across a series of standardized tests. In the acid and alkali resistance test, immersion in 10% HCl and 10% NaOH solutions resulted in a coating rating of 9 or higher—exceeding the national standard requirement of 7 and achieving the highest grade—with no observed black spots, white spots, or peeling after drying. Salt spray testing with a 5% NaCl solution (pH 6.5–7.2) yielded a rating of RtNo10 according to the JIS Z 2371 [43] standard, indicating no significant defects. Similarly, after 120 h of accelerated aging under UV-B exposure and condensation cycles, the coating maintained a corrosion rating of RtNo10. Adhesion was evaluated through cupping, cross-cut, and T-bend tests, all of which showed no coating peeling, with the T-bend test achieving the highest rating of Class 0. This comprehensive performance is attributed to the excellent processability and corrosion resistance of the ETFE coating material. All test results are shown in Figure 2.

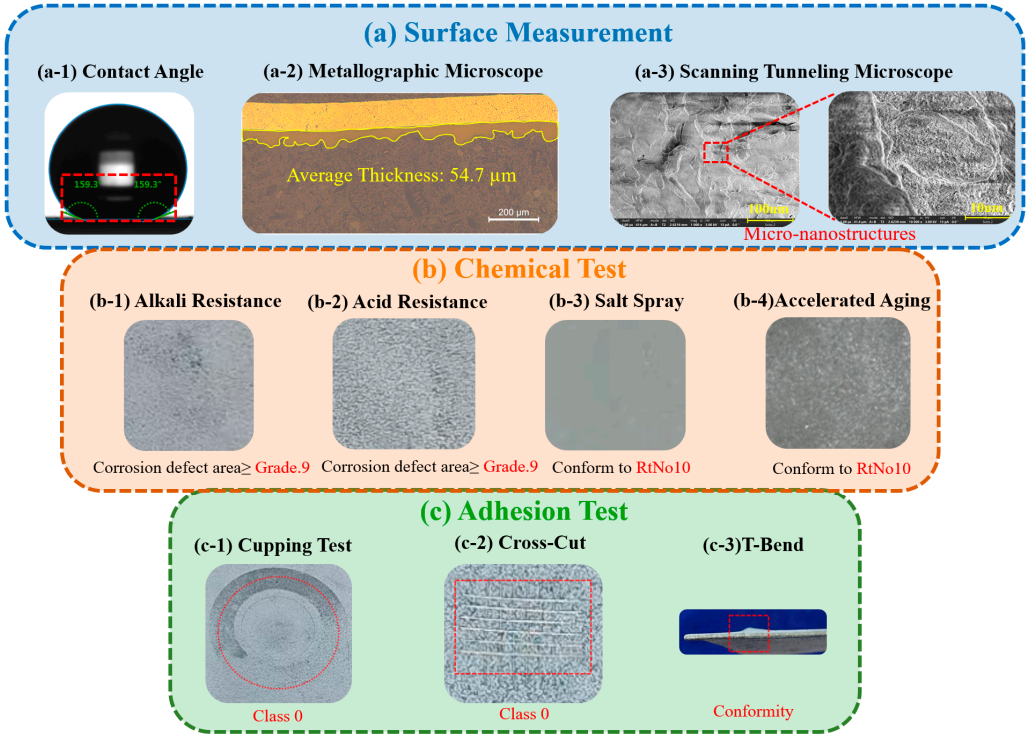


Figure 2. Characterization of the superhydrophobic coating: (**a-1**) water contact angle, (**a-2**) thickness, (**a-3**) SEM morphology; chemical/environmental stability (**b-1**) alkali, (**b-2**) acid, (**b-3**) salt spray, (**b-4**) UV aging; mechanical adhesion (**c-1**) cupping, (**c-2**) cross-cut, (**c-3**) T-bend.

2.4. Experimental Setup and Testing Conditions

The experiments were conducted in an air enthalpy difference laboratory conforming to the Chinese standard GB/T 17758 [44] shown in Figure 3, The facility comprises independent indoor and outdoor environmental chambers capable of precise control over air temperature (−10 to 50 °C) and relative humidity (30% to 95% RH). The air handling units, equipped with heating, humidifying, and cooling systems, maintained temperature and humidity with accuracies of ±0.2 °C and ±1% RH, respectively. Pt100 sensors were installed at the inlets and outlets of the heat exchangers to measure air temperature, while humidity probes monitored humidity levels. All sensors were properly sealed and insulated to minimize measurement error, with data recorded at one-minute intervals.

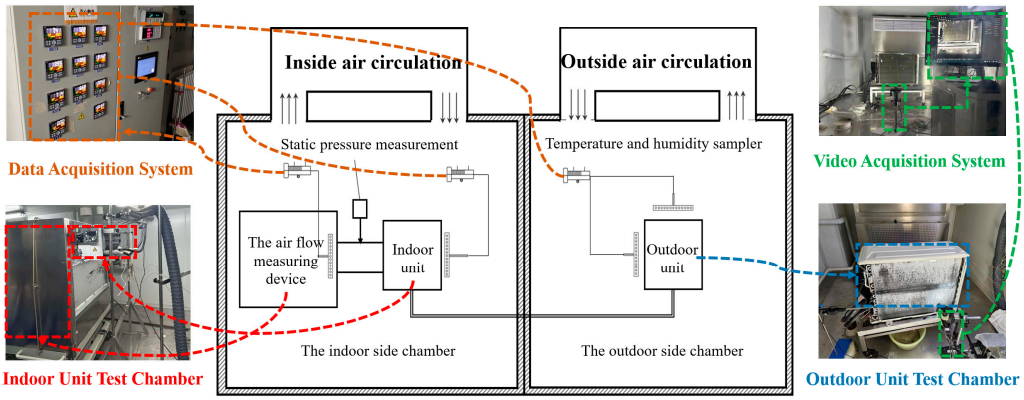


Figure 3. Schematic of the air enthalpy difference laboratory setup with sensor locations and test unit connections.

Performance tests were carried out in accordance with relevant national standards: GB/T 25127.2 [45] for heating mode and GB/T 7725 [46] for cooling mode. The heating

tests were performed under outdoor conditions of 2/1 °C (dry-bulb/wet-bulb) and indoor conditions of 20/15 °C. During heating tests, the indoor unit was set to 30 °C with the fan operating at maximum speed and the auxiliary heater deactivated. Cooling tests were conducted with outdoor conditions of 35/24 °C and indoor conditions of 27/19 °C, with the unit operating in cooling mode at maximum fan speed and a set temperature of 16 °C. Under these controlled conditions, the overall heating and cooling performance of both hydrophilic and superhydrophobic units was systematically evaluated and compared.

The testing of all units was conducted in the same enthalpy difference laboratory, and the unit models are identical. Therefore, it can be confirmed that they share the same control logic, data system algorithms, temperature set points, and sensor placements. The heating capacity and COP values mentioned in the text for the superhydrophobic heat exchanger and the hydrophilic heat exchanger were calculated based on identical startup times, operating durations, and shutdown times.

2.5. Uncertainty Analysis

The experimental uncertainties associated with comparing the hydrophilic and superhydrophobic units stemmed from both operational and systemic sources. Operational uncertainties included: (1) refrigerant charge deviation (±10 g, ±1.25%) resulting from handling and weighing processes; (2) variations in residual non-condensable gas content; (3) the added mass of the superhydrophobic coating (~160 g), which may affect system vibrations; (4) minor installation inconsistencies such as pipe insulation and bending; and (5) physical variations in fin condition. The relatively low data sampling frequency also contributed to operational uncertainty. In contrast, systemic uncertainties—such as those inherent to the enthalpy difference chamber and the data acquisition system—were consistent for both units and thus had a negligible impact on the comparative analysis.

3. Results

3.1. Observation of Frost Completion and Propagation on Hydrophilic and Superhydrophobic Fin Leading Edges

Figure 4 demonstrates the significantly enhanced anti-frosting performance of the superhydrophobic surface under 2/1 °C conditions, delaying frost completion by a factor of 2.83 compared to the hydrophilic surface. Specifically, frost formation began on the hydrophilic surface after approximately 12 min, whereas on the superhydrophobic surface, droplet freezing was postponed until 41 min, initiating predominantly at the fin leading edge and propagating via a freezing wave.

Close inspection also revealed a challenge in applying the electrostatic spray coating to ultra-thin fins (100 μm). Localized coating non-uniformity, observed as substrate exposure, was noted at the fin leading edges. This is attributed to a scale mismatch between the thin fin substrate and the 30~40 μm coating powder, which can hinder effective electrostatic deposition. Furthermore, the freezing behavior exhibited strong size dependence. Micro- and nano-scale droplets, characterized by small volume, low impurity concentration, high surface-to-volume ratio, and significant curvature effects, require a higher energy barrier for homogeneous nucleation, allowing them to remain in a supercooled liquid state for an extended period. Freezing typically occurred only after droplets coalesced and grew beyond a critical size, enabling the formation of stable ice nuclei—a phenomenon clearly illustrated in the 60 min image of the superhydrophobic fins.

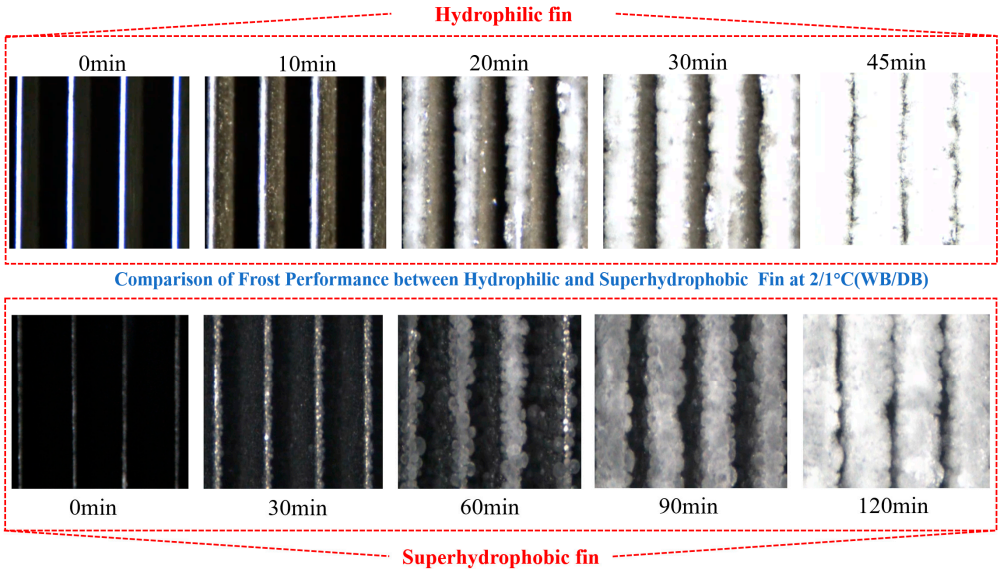


Figure 4. Temporal progression of frost formation on hydrophilic and superhydrophobic fins under low-temperature heating conditions (2/1 °C).

3.2. Defrosting Behavior of Hydrophilic and Superhydrophobic Heat Exchangers

Figure 5 reveals fundamentally different defrosting behavior and frost structure between the superhydrophobic and hydrophilic heat exchangers. The defrosting process on the superhydrophobic surface was significantly accelerated by spontaneous sloughing of the frost layer prior to complete melting, resulting from the critically low frost adhesion force inherent to the low-surface-energy coating. This mechanism allows interfacial meltwater to drain and mechanically dislodge the overlying frost, thereby bypassing the energy-intensive complete phase change required on the hydrophilic surface.

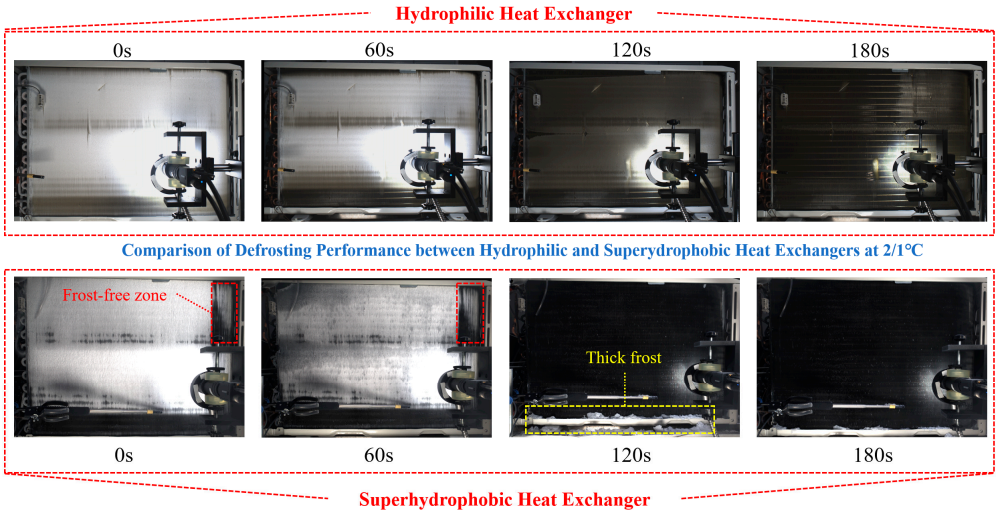


Figure 5. Defrosting progression on hydrophilic and superhydrophobic heat exchangers under low-temperature heating conditions (2/1 °C).

Spatial analysis further identified a distinct frost-free zone in the central, warmer region of the superhydrophobic exchanger, confirming its ability to suppress nucleation where surface supercooling is minimal. Morphologically, the frost on the superhydrophobic surface formed a porous, discontinuous layer with pronounced windward-leeward thickness variation, attributable to localized nucleation and growth conditions. In contrast, the hydrophilic surface promoted a dense, uniform frost layer. Although both frost patterns

degrade thermal–hydraulic performance, the inhomogeneous distribution on the superhydrophobic surface preferentially increases local airflow resistance, while the uniform layer on the hydrophilic surface leads to a more consistent performance reduction across the exchanger.

3.3. Comparison of Key Performance Timings

Figure 6 compares the key performance timings of the hydrophilic and superhydrophobic heat exchangers. The initial frost formation time was determined visually, whereas the frosting completion time and total defrosting duration were identified from characteristic inflection points in the temperature and airflow rate curves.

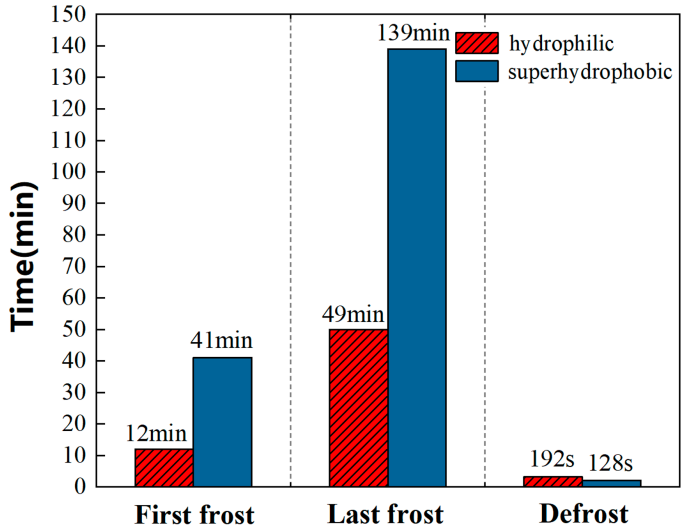


Figure 6. Frosting and defrosting timelines of the hydrophilic and superhydrophobic heat exchangers.

Frost initiated on the hydrophilic surface after 12 min, which is attributed to its high surface energy that significantly reduces the energy barrier for condensation nucleation, thereby promoting rapid and uniform frost layer formation. In contrast, the superhydrophobic surface delayed frost initiation until 41 min, owing to its ultralow surface energy that effectively suppresses droplet freezing. The time to complete frosting was substantially extended to 139 min for the superhydrophobic exchanger—2.83 times longer than that of the hydrophilic exchanger (49 min). During defrosting, the superhydrophobic surface required only 128 s, 33.3% shorter than the 192 s needed for the hydrophilic surface. This acceleration is attributed to the low frost adhesion strength of the superhydrophobic coating, which promotes easy frost shedding.

3.4. Comparison of Low-Temperature Heating Performance Between Hydrophilic and Superhydrophobic Units

In an enthalpy difference laboratory test, the heating capacity Q_H of an air conditioner is calculated by measuring the air parameter changes on the indoor unit side. The calculation formula is as follows:

$$Q_H = m_a \cdot (h_2 - h_1) \quad (1)$$

where

Q_H is the heating capacity of the air conditioner,

m_a is the mass flow rate of air passing through the heat exchanger of the indoor unit, this is a key parameter measured and calculated by devices such as the nozzle flow meter in the enthalpy difference laboratory.

h_2 is the specific enthalpy of moist air at the outlet of the indoor unit.

h_1 is the specific enthalpy of moist air at the inlet of the indoor unit.

During heating operation, the heat exchanger of the indoor unit acts as a condenser, releasing heat to the indoor air. Therefore, the enthalpy of the air increases after passing through it ($h_2 > h_1$). The product of this enthalpy increase and the air mass flow rate represent the heat delivered by the air conditioner to the indoor space, i.e., the heating capacity. In the enthalpy difference test, the specific enthalpies of the air at the inlet and outlet can be calculated based on the measured dry-bulb temperatures, wet-bulb temperatures, and atmospheric pressure at the inlet and outlet of the indoor unit.

The coefficient of performance is an indicator of heating efficiency, defined as the ratio of heating capacity to total input power. The calculation formula is as follows:

$$COP_h = \frac{Q_H}{W_{total}} \tag{2}$$

where COP_h is the heating coefficient of performance, a dimensionless number. W_{total} is the total input power of the air conditioner, in W. This refers to the total active power consumed from the grid by the air conditioning system during heating operation.

Figure 7 shows distinct performance trends between the two units during the early frosting stage (t < 35 min). The hydrophilic unit maintained a higher heating capacity initially, peaking at 4314 W (COP_{hmax} = 2.83) at 24 min. This is attributed to its high surface energy, which promotes more condensation nucleation sites and enhances early heat transfer. However, as frost accumulated, the increased airflow resistance and thermal resistance led to a gradual performance decline.

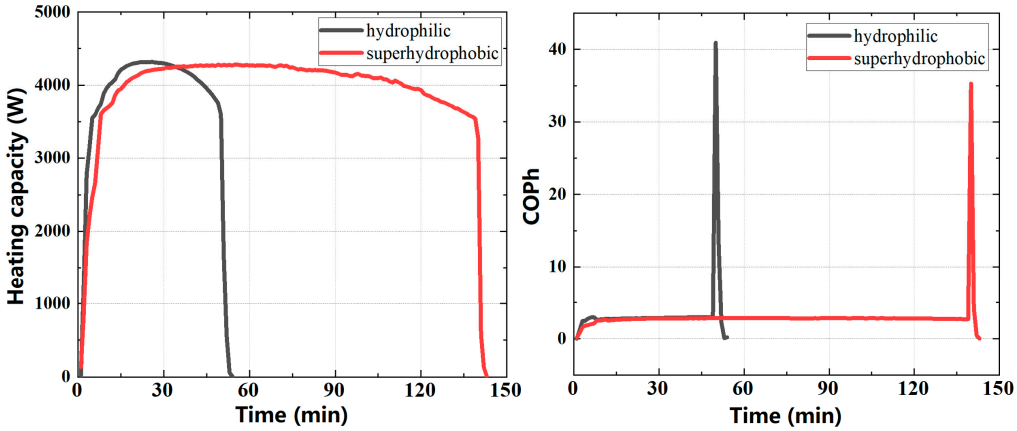


Figure 7. Temporal evolution of heating capacity and COP_h for the hydrophilic and superhydrophobic units.

In contrast, the superhydrophobic unit started with a lower heating capacity but demonstrated sustained performance due to effective frost suppression. It reached a similar peak capacity of 4283 W (COP_{hmax} = 2.82) at 55 min, with a slower subsequent decay. A notable difference was observed in defrost initiation: the hydrophilic unit began defrosting at 49 min, accompanied by sharp drops in airflow and power, and significant COP fluctuations. The superhydrophobic unit delayed defrosting until 139 min, highlighting its strong frost-delaying capability and extended operation.

Based on the experimental data, the following key performance indicators were determined: the average heating capacity (Q_{AH}), the frosting duration (T_c), the defrosting duration (T_d), and the average coefficient of performance (COP_{Ah}). The results are summarized in Table 1.

Table 1. Comparison of key performance parameters between the hydrophilic and superhydrophobic heat exchangers.

Parameter	Hydrophilic Unit	Superhydrophobic Unit
Frosting duration, T_c (min)	49	139
Defrosting duration, T_d (s)	192	128
Average coefficient of performance, COP_{Ah}	2.787	2.724
Average heating capacity, Q_{AH} (W)	3951.49	4004.89

Owing to the significantly longer frosting-defrosting cycle ($T_c + T_d$) of the superhydrophobic heat exchanger compared to its hydrophilic counterpart, two evaluation metrics—defrosting frequency (f_d) and defrosting time benefit (t_h)—are introduced to quantify its performance advantage.

The defrosting frequency, defined as the number of defrost cycles per hour, is calculated as

$$f_d = \frac{60}{T_c} \tag{3}$$

where T_c is the frosting duration in minutes. This metric reflects how often defrosting is required.

The defrosting time benefit (t_h) represents the net effective operating time saved by the superhydrophobic exchanger within one full cycle of the hydrophilic unit, primarily due to its slower frosting and faster defrosting. It is calculated as

$$t_h = \left(\frac{T_c + T_d}{T_{ci} + T_{di}} - 1 \right) \times (2 \times T_{di} - T_d) \tag{4}$$

where T_{ci} and T_{di} are the frosting and defrosting durations of the hydrophilic heat exchanger, respectively.

To facilitate comparison under the assumption of zero heating capacity during defrosting, the average heating capacity (Q_{AHh}) and the average coefficient of performance (COP_{Ahh}), corrected for the time benefit, are defined as follows:

$$Q_{AHh} = (1 + \frac{t_h}{T_c}) Q_{AH} \tag{5}$$

$$COP_{Ahh} = (1 + \frac{t_h}{T_c}) COP_{Ah} \tag{6}$$

These corrected values represent the effective average heating capacity and COP of the superhydrophobic heat exchanger, accounting for the gain in operational time resulting from its prolonged frosting cycle and reduced defrosting duration. The results are summarized in Table 2.

Table 2. Defrosting frequency, effective heating time benefit, and corresponding performance metrics.

Parameter	Hydrophilic Unit	Superhydrophobic Unit
Defrosting frequency, f_d (Hz)	1.22	0.43
Defrosting time benefit, t_h (min)	0	7.27
Adjusted average heating capacity, COP_{Ahh}	2.787	2.866
Adjusted average COP, Q_{AHh} (W)	3951.49	4214.48
Relative improvement in, Q_{AHh}	0	6.24%
Relative improvement in, COP_{Ahh}	0	2.83%

In summary, after adjusting for the defrosting time benefit, the superhydrophobic heat exchanger exhibits a 6.24% increase in the average heating capacity and a 2.83% improvement in the average COP compared to the hydrophilic unit. This enhancement is primarily attributed to the significantly extended frosting time of the superhydrophobic

surface, which effectively reduces the frequency of defrost cycles, consequently improving the overall average heating performance.

3.5. Comparison of Free Cooling Performance Between Hydrophilic and Superhydrophobic Units

As illustrated in Figure 8, the cooling capacity of both units exhibits distinct periodic fluctuations, indicating an intermittent operation mode. Throughout the test, the hydrophilic heat exchanger demonstrated higher peak and average cooling capacities compared to its superhydrophobic counterpart. This performance discrepancy is attributed to the heat transfer mechanism during the cooling cycle, where the outdoor unit acts as a condenser releasing heat to the environment without phase change. Under this condition, heat transfer performance is predominantly governed by convective and conductive thermal resistances. Given the identical outdoor fan speed, the convective resistance was comparable for both units. Thus, the key difference stems from the additional conductive resistance introduced by the functional coatings. In this experiment, the thickness of the superhydrophobic coating (54.7 μm) was significantly greater than that of the hydrophilic coating (2.0 μm), resulting in a notably higher conductive thermal resistance and, consequently, a lower heat exchange efficiency for the condenser equipped with the superhydrophobic coating.

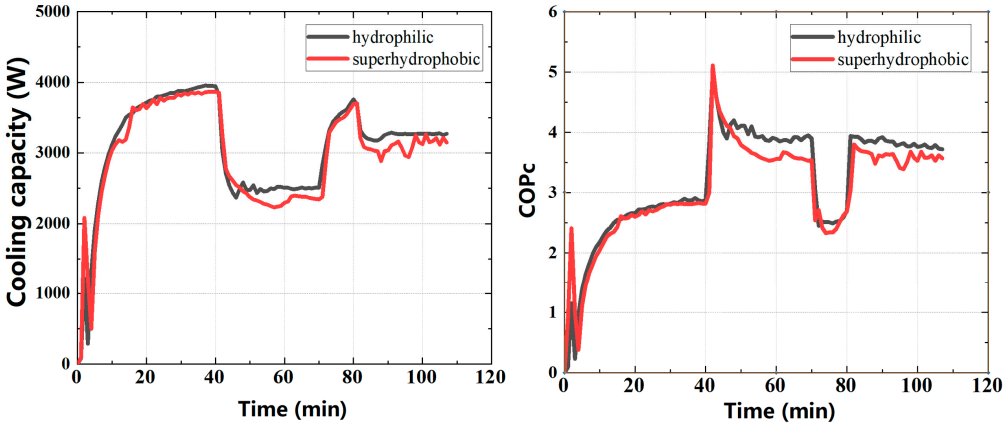


Figure 8. Temporal variation in the cooling capacity and COP_c for hydrophilic and superhydrophobic units.

Based on the data presented in Figure 8, the key performance parameters were calculated, including the average cooling capacity (Q_{AC}) and the average cooling coefficient of performance (COP_{Ac}). The results are summarized in Table 3.

Table 3. Comparison of average cooling performance parameters between hydrophilic and superhydrophobic heat exchangers under free-cooling conditions.

Parameter	Hydrophilic Unit	Superhydrophobic Unit
Average cooling capacity, Q_{AC} (W)	3121.47	3024.20
average cooling COP, COP_{Ac}	3.252	3.105
Relative change in Q_{AC}	0	−3.1%
Relative change in COP_{Ac}	0	−4.5%

In summary, the superhydrophobic coating applied via electrostatic spraying, with a thickness of 54.7 μm (approximately 27 times thicker than the 2 μm hydrophilic coating), introduced significantly higher conductive thermal resistance. This consequently led to a 3.1% reduction in the average cooling capacity and a decrease of 4.5% in the COP compared to the hydrophilic unit. The relatively modest performance degradation, despite the substantial difference in coating thickness, indicates that convective thermal resistance

dominates the total thermal resistance in the free-cooling cycle. This implies that the additional conductive resistance imposed by the functional coating plays a secondary role in overall system performance under these conditions.

It should be noted that this study still has several limitations. First, in terms of the preparation process, the consistency and reliability of the superhydrophobic coating prepared by the electrostatic spraying process on the surface of the heat exchanger require further verification. Second, the scalability of this process also needs to be examined: this study only conducted experiments on a single-row heat exchanger, and its applicability to multi-row or complex-structured heat exchangers in actual large-scale units requires further research for confirmation. Additionally, limited by the high comprehensive cost of enthalpy difference laboratory testing, this study did not conduct multiple repeated tests to evaluate the uncertainty introduced by human error. Therefore, the associated uncertainty was not incorporated into the analysis of the final performance data. In subsequent work, we can enhance coating uniformity and reduce thermal resistance by improving process consistency and further optimizing parameters such as electrostatic spraying powder size, curing temperature, and curing time. The preparation of a superhydrophobic coating with a thickness comparable to that of hydrophilic coatings will further improve the overall performance of the system.

4. Discussion

These results indicate that applying a superhydrophobic coating to the heat pump's outdoor heat exchanger confers considerable advantages. The coating significantly prolongs the time to complete frosting and shortens the defrosting duration under low-temperature, high-humidity conditions. This enhancement stems from the synergistic frost suppression effect of the coating's low surface energy and its micro/nano structure [14–16]. We also found a distinct difference in frosting behavior between the superhydrophobic exchanger and its commercial hydrophilic counterpart. Frost on the superhydrophobic surface mainly formed along the fin thickness direction on the windward side, leaving part of the inner fin area unfrosted, whereas the hydrophilic exchanger was uniformly and entirely frosted. The freezing wave propagated along the fin thickness direction, where the condensed droplets were larger than those along the fin length direction. The initial freezing also preferentially occurred there, likely because the thinner base material in this region made it difficult for electrostatic spraying to achieve a perfectly uniform coating.

While this research primarily aims to improve the performance of residential air-source heat pumps in low-temperature heating, its conclusions are also relevant to other heat pump systems operating in cold, humid environments. Frost formation is a key challenge limiting the widespread use of air-source heat pumps in cold regions [1–3], and this work provides a potential solution. However, given the current limitations of electrostatic spraying powder size, there remains considerable scope for optimizing the coating's average thickness and uniformity, particularly along the fin thickness direction. If a complete, uniform superhydrophobic coating with a thickness similar to hydrophilic coatings can be achieved, it should further extend the frosting cycle, shorten defrosting time, and maintain the original heat transfer performance.

It should be noted that the commercial application of superhydrophobic coatings still faces multiple challenges. For residential heat pumps, the cost must be competitive with hydrophilic coatings, and the conditions for industrial-scale production need to be mature. Additionally, the unique condensation and frosting characteristics of the superhydrophobic surface require corresponding adjustments and optimizations to the traditional heat pump's system structure, flow path design, and control logic to maximize energy-saving benefits through multi-objective coordination For example, based on the unique characteristics

of superhydrophobic heat exchangers, the heat exchange performance can be improved through structural optimization or more intelligent control logic [47,48].

5. Conclusions

This study innovatively applied an electrostatic spraying technique to fabricate a superhydrophobic coating on air-source heat pump heat exchangers. A comparative analysis was conducted against a widely used hydrophilic coating, evaluating their performance under low-temperature heating and free-cooling conditions using a 1.5 HP residential air conditioning unit. The main conclusions are as follows:

Superior Coating Properties and Durability: The electrostatically sprayed superhydrophobic coating demonstrated superior comprehensive performance, significantly outperforming the conventional hydrophilic coating. It achieved the highest grade in standardized tests for adhesion, and resistance to acid, alkali, salt spray, and aging, confirming its exceptional durability and meeting national standards.

Enhanced Frost Suppression and Defrosting Efficiency: The superhydrophobic heat exchanger exhibited remarkable frost retardation and defrosting capabilities. Its frosting duration was extended to 139 min, 2.83 times longer than that of the hydrophilic unit (49 min). The defrosting time was also reduced by 33.3% (128 s vs. 192 s). Frost distribution observations revealed that frost primarily accumulated on the windward side of the superhydrophobic surface, leaving a frost-free area leeward, whereas frost formed uniformly on the hydrophilic surface.

Moderate Impact on Cooling Performance: Under low-temperature heating conditions, after accounting for the defrosting time benefit, the superhydrophobic heat exchanger achieved an average heating capacity of 4214.48 W and an average COP of 2.866. This represents a 6.24% increase in heating capacity and a 2.83% improvement in COP compared to the hydrophilic unit (3951.49 W, COP of 2.787). The performance enhancement is primarily attributed to the significantly extended frosting cycle, which drastically reduces the frequency of defrosting interruptions.

Limited Performance Degradation in Cooling Mode: During free-cooling operation, the superhydrophobic heat exchanger experienced a modest decrease in performance, with a 3.1% reduction in average cooling capacity (3024.20 W vs. 3121.47 W) and a 4.5% reduction in average COP (3.105 vs. 3.252) compared to the hydrophilic unit. This degradation is attributed to the greater thickness of the superhydrophobic coating (54.7 μm versus 2 μm), which introduces additional conductive resistance. However, the relatively small magnitude of this performance loss indicates that convective thermal resistance remains the dominant factor governing heat transfer in the condensation-based cooling mode, thereby marginalizing the impact of the coating's conductive resistance.

Author Contributions: S.F.: data curation, formal analysis, investigation, visualization, writing—original draft. Z.D.: formal analysis, investigation, visualization, writing—editing. Z.K.: supervision, funding acquisition. D.Z.: supervision, writing—review. Z.Y.: conceptualization, writing—review, funding acquisition. All authors have read and agreed to the published version of the manuscript.

Funding: This work was supported by the National Natural Science Foundation of China (Grant No. 12202235) and Jiangxi Provincial Natural Science Foundation (No. 20232BAB204057).

Data Availability Statement: The data that support the findings of this study are available within the article.

Conflicts of Interest: The authors have no conflicts to disclose.

Abbreviations and Symbols

The following abbreviations and symbols are used in this manuscript:

ASHPs	Air-source heat pumps
COP	coefficient of performance
ETFE-F-SiO_2	ETFE-Fluorine modified SiO_2
Q_H	the heating capacity of the air conditioner, W
m_a	the mass flow rate of air passing, kg/s
h_2	the specific enthalpy of moist air at the outlet of the indoor unit, kJ/kg
h_1	the specific enthalpy of moist air at the inlet of the indoor unit, kJ/kg
COP_h	Coefficient of Performance for heating
COP_{hmax}	Maximum Coefficient of Performance for heating
T_c	Frosting duration, s
T_d	Defrosting duration, s
T_{ci}	Frosting durations of the hydrophilic heat exchanger, s
T_{di}	Defrosting durations of the hydrophilic heat exchanger, s
COP_{Ah}	Average COP for heating
Q_{AH}	Average heating capacity, W
f_d	Defrosting frequency, Hz
t_h	Defrosting time benefit, s
COP_{Ahh}	Adjusted average COP for heating
Q_{AHh}	Adjusted average heating capacity
Q_{Ac}	Average cooling capacity
COP_{Ac}	Average COP for cooling

References

1. Sun, H.; He, H.; Lyu, N.; Wang, F.; Liang, C.; Zhang, X. Experimental Study of Active–Passive Defrosting Strategy for Heat Exchangers with Superhydrophobic Surface Modification. *Appl. Therm. Eng.* **2025**, *280*, 128484. [CrossRef]
2. Lin, Y.; Wang, W.; Luo, J.; Wang, S.; Wei, W.; Luo, Q.; Sun, Y.; Dai, C. Advances in Frosting Suppression Air Source Heat Pump Device: Definition and Classification. *Energy Build.* **2025**, *348*, 116455. [CrossRef]
3. Ikram, H.; Ali, J.; Alexander, A.; Bach, C.K. Optimal Heat Pump Defrosting Strategies for Full-Cycle Capacity and COP Maximization. *Energy* **2025**, *336*, 138302. [CrossRef]
4. Jang, J.Y.; Bae, H.H.; Lee, S.J.; Ha, M.Y. Continuous Heating of an Air-Source Heat Pump during Defrosting and Improvement of Energy Efficiency. *Appl. Energy* **2013**, *110*, 9–16. [CrossRef]
5. Essadik, M.; Hajabdollahi Ouderji, Z.; McKeown, A.; Lu, Y.; Yu, Z. A Multi-Valve Flexible Heat Pump System with Latent Thermal Energy Storage for Defrosting Operation. *Energy Build.* **2024**, *321*, 114656. [CrossRef]
6. Tang, Y.; Liu, Z.; Li, L.; Tang, Y.; Liu, Z.; Li, L. Performance Comparison of a Distributed Energy System under Different Control Strategies with a Conventional Energy System. *Energies* **2019**, *12*, 4613. [CrossRef]
7. Long, Z.; Jiankai, D.; Yiqiang, J.; Yang, Y. A Novel Defrosting Method Using Heat Energy Dissipated by the Compressor of an Air Source Heat Pump. *Appl. Energy* **2014**, *133*, 101–111. [CrossRef]
8. Hu, B.; Yang, D.; Cao, F.; Xing, Z.; Fei, J. Hot Gas Defrosting Method for Air-Source Transcritical CO_2 Heat Pump Systems. *Energy Build.* **2015**, *86*, 864–872. [CrossRef]
9. Amer, M.; Wang, C.-C. Review of Defrosting Methods. *Renew. Sustain. Energy Rev.* **2017**, *73*, 53–74. [CrossRef]
10. Li, Z.-L.; Zhang, C.-L.; Liu, H.-M.; Wang, X.-C. Feasibility Analysis of Thermal Storage Defrosting Method for Air Source Heat Pump: From Energetic and Economic Viewpoints. *Appl. Therm. Eng.* **2024**, *236*, 121828. [CrossRef]
11. Maddah, S.; Goodarzi, M.; Safaei, M.R. Comparative Study of the Performance of Air and Geothermal Sources of Heat Pumps Cycle Operating with Various Refrigerants and Vapor Injection. *Alex. Eng. J.* **2020**, *59*, 4037–4047. [CrossRef]
12. Sui, Y.; Sui, Z.; Liang, G.; Wu, W.; Sui, Y.; Sui, Z.; Liang, G.; Wu, W. Superhydrophobic Microchannel Heat Exchanger for Electric Vehicle Heat Pump Performance Enhancement. *Sustainability* **2023**, *15*, 13998. [CrossRef]
13. Peng, J.; Wang, X.; Zhou, J.; Wang, J.; Yang, Y.; Mei, Y. Photothermal/Electrothermal Superhydrophobic Composite Coating for Efficient Anti-Icing and de-Icing. *Compos. Part B Eng.* **2026**, *310*, 113144. [CrossRef]
14. Huang, W.; Huang, J.; Guo, Z.; Liu, W. Icephobic/Anti-Icing Properties of Superhydrophobic Surfaces. *Adv. Colloid Interface Sci.* **2022**, *304*, 102658. [CrossRef]

15. Luo, J.; Guo, Z. Recent Advances in Biomimetic Superhydrophobic Surfaces: Focusing on Abrasion Resistance, Self-Healing and Anti-Icing. *Nanoscale* **2024**, *16*, 16404–16419. [CrossRef]
16. Liu, Q.; Tang, A.; Wang, Z.; Zhao, B. Exploring the Road Icing Risk: Considering the Dependence of Icing-Inducing Factors. *Nat. Hazards* **2023**, *115*, 2161–2178. [CrossRef]
17. Xu, Y.; Wang, F.; Zhang, Y.; Shu, T.; Huang, W.; Yan, X.; Lei, Y.; Liu, S.; Chen, X. Robust Photo/Electrothermal Synergistically All-Weather Anti/de-Icing Superhydrophobic Composite Coating Based on Modified Graphene. *Colloids Surf. Physicochem. Eng. Asp.* **2025**, *716*, 136699. [CrossRef]
18. Mao, M.; Wei, J.; Li, B.; Li, L.; Huang, X.; Zhang, J. Scalable Robust Photothermal Superhydrophobic Coatings for Efficient Anti-Icing and de-Icing in Simulated/Real Environments. *Nat. Commun.* **2024**, *15*, 9610. [CrossRef] [PubMed]
19. Yang, X.; Liu, Y.; Zhong, Y.; Chen, H. Ultra-Durable Photothermal Anti-/de-Icing Superhydrophobic Coating with Water Droplets Freezing from the Outside In. *J. Colloid Interface Sci.* **2025**, *682*, 1127–1139. [CrossRef]
20. Zheng, X.; Zhang, H.; Chen, B.; Shen, H.; Li, L.; Ju, G. Flexible and Longterm Superhydrophobic Coating for Anti-Icing and Photothermal de-Icing. *Prog. Org. Coat.* **2026**, *211*, 109729. [CrossRef]
21. Ma, T.; Wei, J.; Sun, W.; Zhang, S.; Wang, D.; Yang, X.; Zhou, Z.; Tong, W.; Wang, J. Durable Photothermal Superhydrophobic Coatings with Amorphous-Polymer Composite Structure Enhance Anti-Icing and Environment-Resistant Properties. *Langmuir* **2025**, *41*, 29051–29063. [CrossRef]
22. Ge-Zhang, S.; Yang, H.; Ni, H.; Mu, H.; Zhang, M. Biomimetic Superhydrophobic Metal/Nonmetal Surface Manufactured by Etching Methods: A Mini Review. *Front. Bioeng. Biotechnol.* **2022**, *10*, 958095. [CrossRef]
23. Sun, X.; Li, Y.; Xie, L.; Pang, C.; Sun, Y.; Luo, K.; Tian, M.; Wang, F. Research on the Preparation Process of Superhydrophobic Titanium Alloy Surface Using Picosecond Laser. *J. Mater. Eng. Perform.* **2025**. [CrossRef]
24. Long, C.; Jinghang, X.; Xichun, L.; Zhanqiang, L.; Bing, W.; Qinghua, S.; Yukui, C.; Yi, W.; Xiangyu, G.; Chunlong, L. Micro/Nano Manufacturing Aircraft Surface with Anti-Icing and Deicing Performances: An Overview. *Nanotechnol. Rev.* **2023**, *12*, 20230105. [CrossRef]
25. Li, H.; Xin, L.; Zhang, K.; Yin, X.; Yu, S. Fluorine-Free Fabrication of Robust Self-Cleaning and Anti-Corrosion Superhydrophobic Coating with Photocatalytic Function for Enhanced Anti-Biofouling Property. *Surf. Coat. Technol.* **2022**, *438*, 128406. [CrossRef]
26. Jiang, L.; Yang, J.; Wu, C.; Wang, X.; Feng, J.; Zhang, R.; Zhang, W.; Kong, X. Fabrication of a Robust Superhydrophobic Coating Exhibiting Superior Corrosion Resistance via Spray Application Technique. *Colloids Surf. Physicochem. Eng. Asp.* **2024**, *687*, 133497. [CrossRef]
27. Fan, X.; Song, S.; Shi, Y.; Cai, M.; Huang, Y.; Zhang, B.; Zhu, M. Mechanochemical Stable Superhydrophobic Coating toward Lasting Corrosion Protection. *Prog. Org. Coat.* **2023**, *178*, 107478. [CrossRef]
28. Cao, Y.; Cheng, H.; Gu, N.; Ou, K.; Wang, Z.; Liu, Q.; Guan, R.; Fu, Q.; Sun, Y. Excellent Mechanical Durability of Superhydrophobic Coating by Electrostatic Spraying. *Mater. Chem. Phys.* **2023**, *301*, 127658. [CrossRef]
29. Hou, X.; Ou, J.; Li, C.; Hu, Y.; Wang, F.; Fang, X.; Li, W.; Amirfazli, A. Electrostatic Spraying of Zinc Carbonate Hydroxide-Infused Ethylene-Tetrafluoroethylene Powders: A Thermally-Induced, VOC-Free Antibacterial Superhydrophobic Coating. *Colloids Surf. Physicochem. Eng. Asp.* **2025**, *705*, 135569. [CrossRef]
30. Luo, H.; Li, Y.; Huan, D.; Zhu, C.; Wang, J.; Zeng, D. Efficient Fabrication of Wear-Resistant PEEK Matrix Composite Coating with Superhydrophobicity for Self-Cleaning and Anti-Icing Applications. *Polym.-Plast. Technol. Mater.* **2021**, *60*, 1106–1121. [CrossRef]
31. Fang, S.-K.; Li, H.-R.; Feng, S.-D.; Wang, P.-X.; Yu, Y.; Zhang, H.; Guo, J. Cellulose Acetate Superhydrophobic Coatings for Efficient Oil–Water Separation Using a Combination of Electrostatic Spraying and Chemical Vapor Deposition. *Polym. Eng. Sci.* **2023**, *64*, 254–263. [CrossRef]
32. Pan, S.; Wang, N.; Xiong, D.; Deng, Y.; Shi, Y. Fabrication of Superhydrophobic Coating via Spraying Method and Its Applications in Anti-Icing and Anti-Corrosion. *Appl. Surf. Sci.* **2016**, *389*, 547–553. [CrossRef]
33. Liu, M.; Zhang, Y.; Lei, T.; Lin, S.; Cai, X.; Fang, Y. Synergistic Effect of Substrate Heating and Coupling Agent on Electrosprayed Superhydrophobic Coatings. *Prog. Org. Coat.* **2025**, *208*, 109546. [CrossRef]
34. Ganesan, P.; Vanaki, S.M.; Thoo, K.K.; Chin, W.M. Air-Side Heat Transfer Characteristics of Hydrophobic and Super-Hydrophobic Fin Surfaces in Heat Exchangers: A Review. *Int. Commun. Heat Mass Transf.* **2016**, *74*, 27–35. [CrossRef]
35. Bharathidasan, T.; Kumar, S.V.; Bobji, M.S.; Chakradhar, R.P.S.; Basu, B.J. Effect of Wettability and Surface Roughness on Ice-Adhesion Strength of Hydrophilic, Hydrophobic and Superhydrophobic Surfaces. *Appl. Surf. Sci.* **2014**, *314*, 241–250. [CrossRef]
36. Wang, F.; Liang, C.; Yang, M.; Fan, C.; Zhang, X. Effects of Surface Characteristic on Frosting and Defrosting Behaviors of Fin-Tube Heat Exchangers. *Appl. Therm. Eng.* **2015**, *75*, 1126–1132. [CrossRef]
37. Boyina, K.S.; Mahvi, A.J.; Chavan, S.; Park, D.; Kumar, K.; Lira, M.; Yu, Y.; Gunay, A.A.; Wang, X.; Miljkovic, N. Condensation Frosting on Meter-Scale Superhydrophobic and Superhydrophilic Heat Exchangers. *Int. J. Heat Mass Transf.* **2019**, *145*, 118694. [CrossRef]

38. *GB/T 9274-1988*; Paints and Varnishes-Determination of Resistance to Liquids. Standardization Administration of China: Beijing, China, 1988.
39. *GB/T 10125-2021*; Corrosion Tests in Artificial Atmospheres—Salt Spray Tests. Standardization Administration of China: Beijing, China, 2021.
40. *GB/T 16422.3-2022*; Plastics—Methods of Exposure to Laboratory Light Sources—Part 3: Fluorescent UV Lamps. Standardization Administration of China: Beijing, China, 2022.
41. *GB/T 4156-2020*; Metallic Materials—Sheet and Strip—Erichsen Cupping Test. Standardization Administration of China: Beijing, China, 2020.
42. *GB/T 9286-2021*; Paints and Varnishes—Cross-Cut Test. Standardization Administration of China: Beijing, China, 2020.
43. *JIS Z 2371:2015*; Methods of Salt Spray Testing. Japanese Standards Association: Tokyo, Japan, 2015.
44. *GB/T 17758-2023*; Unitary Air Conditioners. Standardization Administration of China: Beijing, China, 2020.
45. *GB/T 25127.2-2020*; Low Ambient Temperature Air Source Heat Pump (Water Chilling) Packages—Part 2: Heat Pump (Water Chilling) Packages for Household and Similar Application. Standardization Administration of China: Beijing, China, 2020.
46. *GB/T 7725-2022*; Room Air Conditioner. Standardization Administration of China: Beijing, China, 2020.
47. Zhu, X.; Zuo, Z.; Wang, W.; Jia, B.; Liu, R.; Yin, Q.; Zhang, M. Performance Comparison and Optimization of Thermoelectric Generator Systems with/without Stepped-Configuration. *Energy* **2025**, *335*, 137924. [CrossRef]
48. Zhu, X.; Zuo, Z.; Wang, W.; Zhang, M.; Yin, Q.; Liu, R.; Jia, B. Transient Modeling and Analysis of a Stepped-Configuration Thermoelectric Generator Considering Non-Uniform Temperature Distribution. *Appl. Energy* **2025**, *383*, 125360. [CrossRef]

Disclaimer/Publisher's Note: The statements, opinions and data contained in all publications are solely those of the individual author(s) and contributor(s) and not of MDPI and/or the editor(s). MDPI and/or the editor(s) disclaim responsibility for any injury to people or property resulting from any ideas, methods, instructions or products referred to in the content.